JOURNAL OF GUIDANCE, CONTROL, AND DYNAMICS
Vol. 31, No. 3, May–June 2008

Attitude Estimation for Sounding Rockets Using Microelectromechanical System Gyros

Jan K. Bekkeng*
University of Oslo, 0316 Oslo, Norway
and
Mark L. Psiaki†
Cornell University, Ithaca, New York 14853-7501

DOI: 10.2514/1.32395

An attitude determination and in-flight calibration extended Kalman filter and the corresponding smoother have been developed to estimate three-axis attitude of spinning sounding rockets. The attitude determination system uses low-accuracy commercial microelectromechanical system rate gyros, coupled with a three-axis magnetometer and a one-axis sun sensor. Because only postflight analysis is necessary, the improved performance of a smoother is used in the attitude reconstruction because postflight computation allows the use of a noncausal algorithm. Gyro misalignment and scale-factor errors are proportional to the angular rate, and spin-stabilized rockets without a despin unit usually have a large angular velocity in the range of 4–6 cycles per second about the spin axis. Therefore, gyro misalignment and scale-factor errors can have a significant effect on the attitude propagation, which is based on the gyro measurements. In this work, in-flight calibration is carried out, estimating sensor relative misalignments in addition to bias and scale-factor errors. To ensure filter convergence, an initialization algorithm suitable for producing an initial attitude estimate from a vector measurement and a scalar measurement has been developed. The initialization algorithm uses an attitude representation based on the minimum quaternion combined with a search method. The filter and smoother have been tested using a truth-model simulation, and the accuracy is shown to be dependent on the rocket motion. A rich motion time history makes the parameters more observable and thereby the estimates more accurate. Simulation results indicate that an attitude accuracy on the order of 0.5–1 degrees (3 sigma) can be achieved with a low-cost suite of sensors.

I. Introduction

THE present work is part of the development of a low-cost attitude determination system (ADS) suitable for sounding rockets. Attitude (orientation) information is required for nearly all space missions, and is necessary to analyze scientific data from sounding rockets. The necessary attitude accuracy depends on the scientific instruments onboard the payload and on the physical conditions during flight. A rocket attitude accuracy of about 1–2 deg is likely to be acceptable in most cases. The system is primarily intended for low-cost sounding rockets without a despin unit. Such fast spinning rockets typically have a nominal spin rate of 4–6 cycles per second (cps) about the roll axis. A typical flight time of sounding rockets is 300–1300 s. The system does not need to determine the attitude in real-time, and so sensor data are transmitted back to ground for postflight attitude determination/reconstruction. This makes possible the use of advanced filtering algorithms, which may be impractical in real-time or in microprocessors onboard the spacecraft. The offline processing makes it possible to run a smoother to obtain more accurate estimates. A smoother produces improved estimates by making use of data both before and after any given time point of interest, which requires a postprocessing scenario to be feasible. This paper treats the problem of estimating the rocket attitude and accomplishing an in-flight calibration of the sensors.

To determine attitude from sensors that provide vector measurements, at least two different vectors are needed at the same time point, except for some special applications [1,2]. With only a single vector measurement, the rotation about this vector cannot be resolved. The attitude solution from vector measurements is the transformation matrix which is determined by matching two nonzero, nonparallel vectors that are known in the reference coordinate frame based on a mathematical model with corresponding vectors that are measured simultaneously in the spacecraft body frame.

The sensor system used in this work consists of a newly developed low-cost inertial reference unit (IRU) that uses commercial microelectromechanical system (MEMS) rate gyros, a three-axis magnetometer (TAM), and a one-axis digital sun sensor (DSS). The data fusion and calibration models are implemented by using an extended Kalman filter (EKF) and an extended Kalman smoother.

The use of the MEMS IRU eliminates the need to use an Euler dynamics model. Only a kinematic model of the attitude propagation is needed, and gyro modeling and calibration become a significant part of the attitude determination problem. The low-accuracy MEMS gyros are improved by detailed preflight calibration and characterization, together with in-flight calibration. The results from the preflight calibration are used in preprocessing the gyro data and in the gyro modeling in the attitude estimator algorithms. In addition to estimating the spacecraft attitude, the filtering and smoothing algorithms also do in-flight calibration to estimate relative sensor misalignment errors, sensor biases, and sensor scale-factor errors. This is important because systematic sensor errors can have a significant effect on the attitude solution [3]. Many of the calibration parameters are difficult to determine preflight, or they may demand high-cost calibration facilities that are not accessible at the payload assembly location. In addition, in-flight calibration is often the only way to estimate realistic calibration parameters for the attitude sensors, after they have been integrated into the payload.

The present work makes four main contributions. First, it demonstrate that the ADS can work with low-performance

Presented as Paper 6382 at the AIAA/AAS Astrodynamics Specialist Conference and Exhibit, Keystone Resort & Conference Center, Keystone, CO, 21–24 August 2006; received 28 May 2007; revision received 14 October 2007; accepted for publication 14 October 2007.

*Scientist, Department of Physics.
†Professor, Sibley School of Mechanical and Aerospace Engineering. Associate Fellow AIAA.

commercial grade MEMS rate gyros, as opposed to navigation grade high-performance gyros. The second contribution is a new sun sensor model for a one-axis digital sun sensor; this model includes bias, scale-factor, and alignment calibration parameters. The third contribution is a new, simple filter initialization strategy, suitable for combining a vector measurement with the scalar sun sensor measurement. The last contribution is a demonstration of the ability to do simultaneous attitude determination and in-flight sensor calibration for the proposed system. This demonstration is based on data from truth-model simulations of sounding rockets.

The organization of this paper proceeds as follows. Section II gives a brief review of attitude kinematics. Section III presents models of the sensors. Section IV develops the multiplicative quaternion extended Kalman filter and smoother for this problem. Section V presents a method to generate an initial estimate to ensure EKF convergence. Section VI discusses methods for evaluating the filter's consistency and observability. Section VII presents simulation results, and the conclusions are given in Sec. VIII.

II. Spacecraft Attitude Kinematics

This section contains a brief review of the attitude kinematics equation of motion, using quaternions to represent attitude. The four element quaternion vector is defined by $\boldsymbol{q} = [\boldsymbol{\varrho}^T \;\; q_4]^T$, with $\boldsymbol{\varrho} = [q_1 \;\; q_2 \;\; q_3]^T = \hat{\boldsymbol{e}} \sin(\theta/2)$ and $q_4 = \cos(\theta/2)$, where the unit vector $\hat{\boldsymbol{e}}$ is the axis of rotation and θ is the angle of rotation [4]. The quaternion $\boldsymbol{q}$ obeys the unit normalization constraint given by $\boldsymbol{q}^T\boldsymbol{q} = 1$. The attitude matrix is related to the quaternion by

$$A(\boldsymbol{q}) = \Xi^T(\boldsymbol{q})\Psi(\boldsymbol{q}) \tag{1}$$

with

$$\Xi(\boldsymbol{q}) = \begin{bmatrix} q_4 I_{3\times 3} + [\boldsymbol{\varrho}\times] \\ -\boldsymbol{\varrho}^T \end{bmatrix} \tag{2}$$

$$\Psi(\boldsymbol{q}) = \begin{bmatrix} q_4 I_{3\times 3} - [\boldsymbol{\varrho}\times] \\ -\boldsymbol{\varrho}^T \end{bmatrix} \tag{3}$$

where $I_{3\times 3}$ is the 3×3 identity matrix and $[\boldsymbol{\varrho}\times]$ is a cross product matrix defined by

$$[\boldsymbol{\varrho}\times] = \begin{bmatrix} 0 & -q_3 & q_2 \\ q_3 & 0 & -q_1 \\ -q_2 & q_1 & 0 \end{bmatrix} \tag{4}$$

The attitude matrix $A(\boldsymbol{q})$ and the quaternion $\boldsymbol{q}$ both parameterize the rotation from inertial reference coordinates to spacecraft body coordinates. The quaternion constraint ensures that the rotation matrix is orthonormal. Successive rotations can be modeled by using quaternion multiplication [5]. In this work, quaternion multiplication is defined using the convention of [6], in which the two quaternions in the multiplication expression appear in the same order as do their corresponding rotation matrices when they are multiplied to form the composite rotation matrix:

$$A(\boldsymbol{q}')A(\boldsymbol{q}) = A(\boldsymbol{q}' \otimes \boldsymbol{q}) \tag{5}$$

The quaternion kinematic equation is given by

$$\dot{\boldsymbol{q}} = \frac{1}{2}\Omega(\boldsymbol{\omega})\boldsymbol{q} \tag{6}$$

where $\boldsymbol{\omega} = [\omega_x \;\; \omega_y \;\; \omega_z]^T$ is the angular rate vector of the spacecraft body relative to inertial space as measured in spacecraft body axes, and

$$\Omega(\boldsymbol{\omega}) = \begin{bmatrix} 0 & \omega_z & -\omega_y & \omega_x \\ -\omega_z & 0 & \omega_x & \omega_y \\ \omega_y & -\omega_x & 0 & \omega_z \\ -\omega_x & -\omega_y & -\omega_z & 0 \end{bmatrix} \tag{7}$$

III. Sensor Models

The sensor models are used to relate the attitude, the attitude rate, and the sensor calibration parameters to the sensor outputs. Misalignment calibration parameters must be defined in terms of a reference frame that is fixed to one of the attitude sensors [7]. Following the lead of Pittelkau [8], the rate gyros are chosen to define that frame. This is because the gyros are the basis for the attitude kinematic model, and the gyro data are continuously available with a very high update frequency. The body frame is defined by the gyro axes corrected for nonorthogonal misalignment (skewness). The magnetometer and sun sensor misalignment relative to the corrected gyro axes can then be modeled and estimated. Therefore, the goal of the attitude estimation algorithm is to determine the attitude of the corrected gyro reference frame with respect to the J2000 Earth-centered inertial (ECI) frame.

A. Inertial Reference Unit Model

The IRU model follows the idea from [8], with some modifications. Because the IRU is treated as the reference sensor, only nonorthogonal misalignment (skewness) is considered. The true angular rate $\boldsymbol{\omega}^b$ in the body frame is related to the measured angular rate $\tilde{\boldsymbol{\omega}}$ in the gyro frame, by

$$\boldsymbol{\omega}^b = S_g\tilde{\boldsymbol{\omega}} - \boldsymbol{\beta} - \boldsymbol{\eta}_v \tag{8}$$

where $\boldsymbol{\beta}$ is the sensor bias (in the body frame) and $\boldsymbol{\eta}_v$ is zero-mean, Gaussian white noise. The misalignment is separated into orthogonal and nonorthogonal parts [8], and the nonorthogonal misalignment and scale-factor error matrix M_g is given by

$$M_g = \begin{bmatrix} \lambda_{gx} & \varepsilon_z & \varepsilon_y \\ 0 & \lambda_{gy} & \varepsilon_x \\ 0 & 0 & \lambda_{gz} \end{bmatrix} \tag{9}$$

where $\boldsymbol{\lambda}_g$ is the three-dimensional vector of gyro scale-factor errors, and $\boldsymbol{\varepsilon}$ is the three-dimensional vector of misalignment errors. Note that the misalignment part of the M_g matrix is not skew symmetric precisely because the three misalignments in the $\boldsymbol{\varepsilon}$ vector represent the amounts by which individual gyro sensing axes fail to be orthogonal to each other; they do not represent misalignment of the entire gyro coordinate system relative to some reference spacecraft coordinate system. Because the orthogonal misalignment is set to zero through definition of the body frame, the misalignment and scale-factor matrix S_g is given by

$$S_g = I + M_g = \begin{bmatrix} 1+\lambda_{gx} & \varepsilon_z & \varepsilon_y \\ 0 & 1+\lambda_{gy} & \varepsilon_x \\ 0 & 0 & 1+\lambda_{gz} \end{bmatrix} \tag{10}$$

Inserting Eq. (10) into Eq. (8) yields

$$\boldsymbol{\omega}^b = (I + M_g)\tilde{\boldsymbol{\omega}} - \boldsymbol{\beta} - \boldsymbol{\eta}_v = \tilde{\boldsymbol{\omega}} + \Omega_g\boldsymbol{m}_g - \boldsymbol{\beta} - \boldsymbol{\eta}_v \tag{11}$$

where

$$\Omega_g\boldsymbol{m}_g = M_g\tilde{\boldsymbol{\omega}} \tag{12}$$

with

$$\Omega_g = \begin{bmatrix} 0 & \tilde{\omega}_z & \tilde{\omega}_y & \tilde{\omega}_x & 0 & 0 \\ \tilde{\omega}_z & 0 & 0 & 0 & \tilde{\omega}_y & 0 \\ 0 & 0 & 0 & 0 & 0 & \tilde{\omega}_z \end{bmatrix} \quad \text{and} \quad \boldsymbol{m}_g = \begin{bmatrix} \varepsilon_x \\ \varepsilon_y \\ \varepsilon_z \\ \lambda_{gx} \\ \lambda_{gy} \\ \lambda_{gz} \end{bmatrix} \tag{13}$$

B. Sun Sensor Model

The sun sensor used in this work is a lensless pinhole line camera, where the image sensor is a high-speed complementary metal–oxide-semiconductor (CMOS) linear array with 2048×1 pixels with a

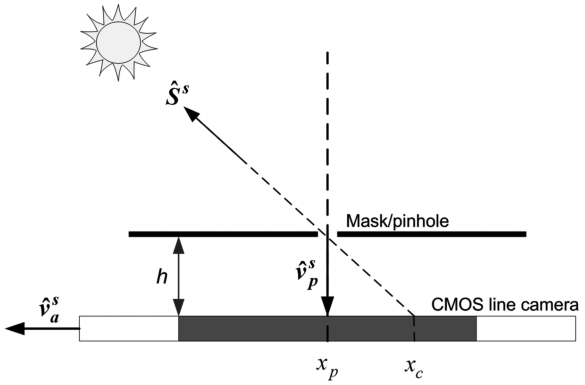

Fig. 1 Sun sensor geometry diagram.

spacing of 7 μm. A pinhole of diameter 0.1 mm is placed 4 mm above the linear image sensor, giving the sun sensor a field of view of approximately 120 deg, see Fig. 1. The sensor is mounted with the detector array aligned parallel to the rocket spin axis, and the sun illuminates different pixels depending on the sun angle (the angle between the spin axis and the pointing vector to the sun). A new sun sensor model had to be developed for this sensor, including the relative orthogonal misalignment between the sun sensor and the corrected gyro axes. The relationship between the sun sensor measurement $\tilde{x}_c$ in the sun sensor frame and the reference sun pointing vector $\hat{\boldsymbol{S}}^{\text{eci}}$ in the ECI frame can be modeled in the following way:

$$\tilde{x}_c = (e_0 + \delta e)\left[\frac{[\hat{\boldsymbol{v}}_a^{s^T} T_b^s A(\boldsymbol{q})\hat{\boldsymbol{S}}^{\text{eci}}][\hat{\boldsymbol{v}}_p^{s^T} T_b^s A(\boldsymbol{q})\hat{\boldsymbol{S}}^{\text{eci}}]}{1 - [\hat{\boldsymbol{v}}_a^{s^T} T_b^s A(\boldsymbol{q})\hat{\boldsymbol{S}}^{\text{eci}}]^2}\right] + b_s + v_{\text{DSS}} \tag{14}$$

where $\tilde{x}_c$ is the measured pixel number of the "optical center" of the sun image on the sensor array, e_0 is the nominal scale factor (in pixels), δe is the scale-factor error (in pixels), b_s is a bias given in pixels, v_{DSS} is white noise, and $\hat{\boldsymbol{v}}_a^{s^T} = [1\ \ 0\ \ 0]$ and $\hat{\boldsymbol{v}}_p^{s^T} = [0\ \ 0\ \ -1]$ are unit vectors in the sun sensor frame. The unit vector $\hat{\boldsymbol{v}}_a^{s^T}$ points along the sensor array, and $\hat{\boldsymbol{v}}_p^{s^T}$ points from the pinhole to the sensor array, at its nearest point to the pinhole. This formula for $\tilde{x}_c$ has been determined by calculating the point on the CMOS line camera that is closest to the vector that extends from the pinhole in the direction of the sun. It is valid even when the sun vector is not exactly in the plane of the pinhole and the CMOS line camera. In the restricted case that constrains the sun vector to lie exactly in this plane, one can use the identity $1 = [\hat{\boldsymbol{v}}_a^{s^T} T_b^s A(\boldsymbol{q})\hat{\boldsymbol{S}}^{\text{eci}}]^2 + [\hat{\boldsymbol{v}}_p^{s^T} T_b^s A(\boldsymbol{q})\hat{\boldsymbol{S}}^{\text{eci}}]^2$ to simplify the bracketed expression in Eq. (14) to the form $[\hat{\boldsymbol{v}}_a^{s^T} T_b^s A(\boldsymbol{q})\hat{\boldsymbol{S}}^{\text{eci}}]/[\hat{\boldsymbol{v}}_p^{s^T} T_b^s A(\boldsymbol{q})\hat{\boldsymbol{S}}^{\text{eci}}]$. This simplified form has not been used to avoid the restriction that the sun vector lie exactly in the plane of the pinhole and the line camera. $\hat{\boldsymbol{S}}^{\text{eci}}$ is calculated from a mathematical model of the sun position. The formula in the Astronomical Almanac [9] is used in this work, and it gives the coordinates of the sun to a precision of 0.01 deg.

The misalignment of the sensor is described by an orthogonal rotation matrix from the sun sensor frame to the body frame that is defined by 1-2-3 Euler rotations:

$$T_s^b = R_3(\psi_s)R_2(\theta_s)R_1(\phi_s) \tag{15}$$

Using small angle approximations, the rotation matrix from the body frame to the sun sensor frame is given by

$$T_b^s = (T_s^b)^T \approx \begin{bmatrix} 1 & -\psi_s & \theta_s \\ \psi_s & 1 & -\phi_s \\ -\theta_s & \phi_s & 1 \end{bmatrix} \tag{16}$$

The nominal scale factor e_0 is related to the distance h (in meters) between the detector array and the pinhole by the relation $e_0 = -c_0 h$, where c_0 is the number of pixels per meter in the sensor array, as determined from the sensor data sheet. From the CMOS sensor manufacturing process, c_0 is expected to be very accurate. Therefore, the scale-factor error δe probably has its main contribution from error in the nominal distance h.

The foregoing model is a one-axis model, which makes it different from most sun sensor models. This instrument could be used to deduce a two-axis measurement if the measurement were recorded only at the time when the measured sun intensity was the brightest on the CMOS line camera. At this point in time, the sun direction vector would be known to lie in the plane of the line camera and the pin hole. This knowledge would provide the second axis of information. It is difficult to precisely measure the time of the highest intensity, however, and this difficulty degrades the possible accuracy of this second axis. Therefore, it has not been deemed worthwhile to try to use this instrument in a two-axis mode.

C. Magnetometer Model

The measured magnetic field $\tilde{\boldsymbol{B}}$ in the magnetometer frame is related to the reference magnetic field $\boldsymbol{B}^{\text{eci}}$ in the ECI frame by

$$\tilde{\boldsymbol{B}} = S_m[A(\boldsymbol{q})\boldsymbol{B}^{\text{eci}} + \boldsymbol{b}] + \boldsymbol{v}_{\text{TAM}} \tag{17}$$

where $\boldsymbol{b}$ is the magnetometer bias and $\boldsymbol{v}_{\text{TAM}}$ is zero-mean Gaussian white noise. The relative misalignment (orthogonal and non-orthogonal) and scale-factor matrix S_m is represented by

$$S_m = \begin{bmatrix} 1 + \lambda_{mx} & \delta_{xy} & \delta_{xz} \\ \delta_{yx} & 1 + \lambda_{my} & \delta_{yz} \\ \delta_{zx} & \delta_{zy} & 1 + \lambda_{mz} \end{bmatrix} \tag{18}$$

where $\boldsymbol{\lambda}_m$ is a three-dimensional vector of magnetometer scale-factor errors and $\boldsymbol{\delta}$ is a six-dimensional vector of relative and absolute magnetometer misalignment angles. The inertial Earth magnetic field vector $\boldsymbol{B}^{\text{eci}}$ is computed using a 10th-order year 2005 International Geomagnetic Reference Field (IGRF) model.

IV. Extended Kalman Filter and Smoother Development

A. Multiplicative Extended Kalman Filter

The multiplicative extended Kalman filter (MEKF) described here is based on material drawn from [6,10,11]. The MEKF approach is the standard method to avoid a singular covariance matrix caused by the quaternion normalization constraint. The basic idea of the MEKF is to compute an unconstrained estimate of three error components, and to use them to update the correctly normalized four-component quaternion to provide a globally nonsingular attitude representation. The true attitude quaternion $\boldsymbol{q}$ is represented by a quaternion product of the estimated quaternion $\hat{\boldsymbol{q}}$ and an error quaternion $\boldsymbol{\delta q}(\boldsymbol{\delta\varrho})$ in the following way

$$\boldsymbol{q} = \boldsymbol{\delta q}(\boldsymbol{\delta\varrho}) \otimes \hat{\boldsymbol{q}} \tag{19}$$

where $\hat{\boldsymbol{q}}$ is the unit-normalized estimated quaternion and $\boldsymbol{\delta q}(\boldsymbol{\delta\varrho})$ is a unit-normalized quaternion representing the rotation from $\hat{\boldsymbol{q}}$ to the true quaternion $\boldsymbol{q}$, parameterized by the vector of its first three components $\boldsymbol{\delta\varrho}$. Because this error quaternion corresponds to a small rotation, the fourth component will be close to unity, and all the attitude information is contained in the three vector components of $\boldsymbol{\delta\varrho}$. The linearized differential equation for the error quaternion $\boldsymbol{\delta q} = [\boldsymbol{\delta\varrho}^T\ \ \delta q_4]^T$ can be shown to be given by [10]

$$\boldsymbol{\delta}\dot{\boldsymbol{\varrho}} = -[\hat{\boldsymbol{\omega}}^b\times]\boldsymbol{\delta\varrho} + \frac{1}{2}\boldsymbol{\delta\omega} \qquad \delta\dot{q}_4 = 0 \tag{20}$$

where Eq. (11) gives the body angular rate estimate $\hat{\boldsymbol{\omega}}^b = \tilde{\boldsymbol{\omega}} + \Omega_g\hat{\boldsymbol{m}}_g - \hat{\boldsymbol{\beta}}$ and the angular rate error is given by

$$\begin{aligned} \boldsymbol{\delta\omega} &= \boldsymbol{\omega}^b - \hat{\boldsymbol{\omega}}^b \\ &= \Omega_g(\boldsymbol{m}_g - \hat{\boldsymbol{m}}_g) - (\boldsymbol{\beta} - \hat{\boldsymbol{\beta}}) - \boldsymbol{\eta}_v \\ &= \Omega_g\Delta\boldsymbol{m}_g - \Delta\boldsymbol{\beta} - \boldsymbol{\eta}_v \end{aligned} \tag{21}$$

with $\Delta \boldsymbol{m}_g$ being the six-dimensional vector of gyro relative misalignment and scale-factor estimation errors and $\Delta \boldsymbol{\beta}$ being the gyro bias estimation error vector.

B. Continuous-Time Process Model

The full 29-element state vector for the filter is given by

$$\mathbf{x} = [\boldsymbol{\delta\alpha}^T \;\; \boldsymbol{\beta}^T \;\; \boldsymbol{m}_g^T \;\; \boldsymbol{m}_m^T \;\; \boldsymbol{b}^T \;\; \boldsymbol{m}_s^T]^T \tag{22}$$

where

$$\begin{aligned}
\boldsymbol{\delta\alpha} &= [\delta\alpha_x, \delta\alpha_y, \delta\alpha_z]^T \\
\boldsymbol{\beta} &= [\beta_x, \beta_y, \beta_z]^T \\
\boldsymbol{m}_g &= [\varepsilon_x, \varepsilon_y, \varepsilon_z, \lambda_{gx}, \lambda_{gy}, \lambda_{gz}]^T \\
\boldsymbol{m}_m &= [\delta_{xy}, \delta_{xz}, \delta_{yz}, \lambda_{mx}, \lambda_{my}, \lambda_{mz}, \delta_{yx}, \delta_{zx}, \delta_{zy}]^T \\
\boldsymbol{b} &= [b_x, b_y, b_z]^T \\
\boldsymbol{m}_s &= [\phi_s, \theta_s, \psi_s, b_s, \delta e]^T
\end{aligned} \tag{23}$$

The first three state components are $\boldsymbol{\delta\alpha} = 2 \cdot \boldsymbol{\delta q}$ and represent small angle approximations of the attitude errors relative to a unit-normalized quaternion estimate that has been propagated using Eq. (6) with the rate as modeled by Eq. (11). Here, $\boldsymbol{\beta}$ is the vector of rate-gyro biases, $\boldsymbol{m}_g$ is the vector of rate-gyro nonorthogonality and scale-factor errors, $\boldsymbol{m}_m$ is the vector of magnetometer alignment and scale-factor errors, $\boldsymbol{b}$ is the magnetometer bias vector, and $\boldsymbol{m}_s$ is the vector that contains the sun sensor calibration parameters.

Equation (21) substituted into Eq. (20) gives the differential equation for the error angles. This results in the following continuous-time linearized state error differential equation:

$$\begin{aligned}
\frac{d}{dt}\begin{bmatrix} \boldsymbol{\delta\alpha} \\ \Delta\boldsymbol{\beta} \\ \Delta\boldsymbol{m}_g \\ \Delta\boldsymbol{m}_m \\ \Delta\boldsymbol{b} \\ \Delta\boldsymbol{m}_s \end{bmatrix} &= \begin{bmatrix} -[\hat{\boldsymbol{\omega}}^b\times] & -I & \Omega_g & 0 & 0 & 0 \\ 0 & 0 & 0 & 0 & 0 & 0 \\ 0 & 0 & 0 & 0 & 0 & 0 \\ 0 & 0 & 0 & 0 & 0 & 0 \\ 0 & 0 & 0 & 0 & 0 & 0 \\ 0 & 0 & 0 & 0 & 0 & 0 \end{bmatrix} \cdot \begin{bmatrix} \boldsymbol{\delta\alpha} \\ \Delta\boldsymbol{\beta} \\ \Delta\boldsymbol{m}_g \\ \Delta\boldsymbol{m}_m \\ \Delta\boldsymbol{b} \\ \Delta\boldsymbol{m}_s \end{bmatrix} \\
&+ \begin{bmatrix} -I & 0 & 0 & 0 & 0 & 0 \\ 0 & I & 0 & 0 & 0 & 0 \\ 0 & 0 & I & 0 & 0 & 0 \\ 0 & 0 & 0 & I & 0 & 0 \\ 0 & 0 & 0 & 0 & I & 0 \\ 0 & 0 & 0 & 0 & 0 & I \end{bmatrix} \cdot \begin{bmatrix} \boldsymbol{\eta}_v \\ \boldsymbol{\eta}_u \\ \boldsymbol{\eta}_g \\ \boldsymbol{\eta}_m \\ \boldsymbol{\eta}_b \\ \boldsymbol{\eta}_s \end{bmatrix}
\end{aligned} \tag{24}$$

This linearized equation takes the form

$$\Delta\dot{\boldsymbol{x}}(t) = F(t)\Delta\boldsymbol{x}(t) + G\boldsymbol{w}(t) \tag{25}$$

where $\Delta\boldsymbol{x}$ is the error state vector and $\boldsymbol{w}$ is the process noise vector. The calibration parameters are modeled in Eq. (24) as random walk variables. This avoids the possibility that the filter's calculated variances for the parameter estimates converge to zero, and time-varying parameters can also be modeled. The process noise spectral density matrix is given by

$$\tilde{Q} = \mathrm{diag}[\sigma_{v_x}^2 \;\; \sigma_{v_y}^2 \;\; \sigma_{v_z}^2 \;\; \sigma_u^2 I_{3\times3} \;\; \sigma_g^2 I_{6\times6} \;\; \sigma_m^2 I_{9\times9} \;\; \sigma_b^2 I_{3\times3} \;\; \sigma_s^2 I_{5\times5}] \tag{26}$$

where diag[ ] denotes a block diagonal matrix. Because of the short flight time of a sounding rocket, all variances except $\sigma_{v_x}^2$, $\sigma_{v_y}^2$, and $\sigma_{v_z}^2$ are set close to zero, to model these parameters as random constants. The time-dependent gyro bias (gyro drift) is mainly related to temperature changes (self-heating effect and change in ambient temperature), and this temperature-driven bias drift is handled by temperature compensation of the gyro outputs. Therefore, the random constant model is sufficient to model the gyro biases for this application.

C. Discretization of the Continuous-Time Process Model

The discrete-time model of the linearized system in Eq. (25) is given by

$$\Delta\boldsymbol{x}_{k+1} = \Phi_k \Delta\boldsymbol{x}_k + \Gamma_k \boldsymbol{w}_k \tag{27}$$

Instead of using a first-order approximation to determine the state transition matrix Φ, the matrix exponential function $\Phi = e^{F\cdot\Delta T}$ is calculated, where ΔT is the sampling interval. Even though the system matrix F is not time invariant, this is a reasonable approximation because the gyro sampling frequency is high enough to keep the estimated angular rate approximately constant over the sampling interval. The discrete-time process covariance matrix Q is related to the continuous-time spectral density matrix $\tilde{Q}$ by the relation [12]

$$\Gamma Q \Gamma^T = \int_0^{\Delta T} \Phi G \tilde{Q} G^T \Phi^T \, \mathrm{d}t \tag{28}$$

Q and Γ can not be determined uniquely, but any pair that is consistent with Eq. (28) will serve well in the estimator. Instead of using a first-order approximation, the matrix exponential function can be used to calculate Q and Γ as follows [10]:

Define

$$A = \begin{bmatrix} -F & G\tilde{Q}G^T \\ 0 & F^T \end{bmatrix} \cdot \Delta T \tag{29}$$

Then determine the matrix exponential of Eq. (29):

$$B = e^A = \begin{bmatrix} B_{11} & B_{12} \\ 0 & B_{22} \end{bmatrix} \tag{30}$$

This gives

$$S = \Gamma Q \Gamma^T = B_{22}^T \cdot B_{12} \tag{31}$$

By choosing $Q = I$, Cholesky factorization can be used to determine Γ.

D. Measurement Model

The magnetometer and sun sensor measurements are modeled using a nonlinear measurement equation of the following form:

$$\boldsymbol{z}_k = \boldsymbol{h}_k(\boldsymbol{x}_k) + \boldsymbol{v}_k \tag{32}$$

where $\boldsymbol{z}_k$ is the measurement vector and $\boldsymbol{v}_k$ is the zero-mean random measurement error vector. Using the models for the magnetometer and sun sensor, the measurement equation becomes

$$z = \begin{bmatrix} \tilde{x}_c \\ \tilde{\boldsymbol{B}} \end{bmatrix} = \begin{bmatrix} h_1 \\ \boldsymbol{h}_2 \end{bmatrix} + \begin{bmatrix} v_{\mathrm{DSS}} \\ \boldsymbol{v}_{\mathrm{TAM}} \end{bmatrix} \tag{33}$$

where

$$\begin{aligned}
h_1 &= (e_0 + \delta e)\left[\frac{[\hat{\boldsymbol{v}}_a^{s^T} T_b^s A(\boldsymbol{q}) \hat{\boldsymbol{S}}^{\mathrm{eci}}][\hat{\boldsymbol{v}}_p^{s^T} T_b^s A(\boldsymbol{q}) \hat{\boldsymbol{S}}^{\mathrm{eci}}]}{1 - [\hat{\boldsymbol{v}}_a^{s^T} T_b^s A(\boldsymbol{q}) \hat{\boldsymbol{S}}^{\mathrm{eci}}]^2}\right] + b_s \\
\boldsymbol{h}_2 &= S_m[A(\boldsymbol{q})\boldsymbol{B}^{\mathrm{eci}} + \boldsymbol{b}]
\end{aligned} \tag{34}$$

and the measurement error covariance matrix R is given by

$$R = \mathrm{diag}[\sigma_{\mathrm{DSS}}^2 \;\; \sigma_{\mathrm{TAM}}^2 I_{3\times3}] \tag{35}$$

The expressions in Eq. (34) are rewritten by using the relations

$$A(\boldsymbol{q}) = A(\boldsymbol{\delta\alpha})A(\bar{\boldsymbol{q}}) \qquad A(\boldsymbol{\delta\alpha}) \approx I - [\boldsymbol{\delta\alpha}\times] \tag{36}$$

Then the partial derivatives are calculated to determine the measurement Jacobian matrix. The formulas for the partial

derivatives are straightforward to compute, but they are lengthy. They have been omitted for the sake of brevity.

E. Filtering

This section highlights some important aspects of the MEKF implementation that add to the standard discrete EKF equations. A review of the standard EKF equations can be found in, e.g., [12]. Because the gyros are sampled at a high frequency, a discrete propagation equation for the attitude quaternion is used. The quaternion propagation can be approximated using [4]

$$\bar{\boldsymbol{q}}_{k+1} = \exp\left[\frac{1}{2}\Omega(\hat{\boldsymbol{\omega}}_k)\Delta T\right]\hat{\boldsymbol{q}}_k \tag{37}$$

where ΔT is the sampling time interval and $\Omega(\hat{\boldsymbol{\omega}})$ from Eq. (7) is computed using the measured rates in Eq. (11), along with the a posteriori rate-gyro calibration parameter estimates. The a posteriori quaternion estimate at sample k is $\hat{\boldsymbol{q}}_k$, and $\bar{\boldsymbol{q}}_{k+1}$ is the a priori quaternion estimate at sample $k+1$. The a priori attitude error angles are $\delta\bar{\boldsymbol{\alpha}}_{k+1} = 0$. The propagation of the other state vector elements is given by setting the a priori values at time $k+1$ equal to the a posteriori values at time k. The covariance propagation is accomplished using the dynamics model in Eq. (27).

The measurement update equation for the error state vector is given by

$$\begin{aligned}\Delta\hat{\boldsymbol{x}}_{k+1} &= K_{k+1}[z_{k+1} - \boldsymbol{h}_{k+1}(\bar{\boldsymbol{x}}_{k+1})]\\ \Delta\hat{\boldsymbol{x}} &\equiv [\delta\hat{\boldsymbol{\alpha}}^T \;\; \Delta\hat{\boldsymbol{\beta}}^T \;\; \Delta\hat{\boldsymbol{m}}_g^T \;\; \Delta\hat{\boldsymbol{m}}_m^T \;\; \Delta\hat{\boldsymbol{b}}^T \;\; \Delta\hat{\boldsymbol{m}}_s^T]^T\end{aligned} \tag{38}$$

where K_{k+1} is the optimal filter gain, z_{k+1} is the measurement vector, and $\boldsymbol{h}_{k+1}(\bar{\boldsymbol{x}}_{k+1})$ is the predicted measurement vector. From Eq. (19), the small angle approximations $\delta\boldsymbol{\varrho} = 1/2 \cdot \delta\boldsymbol{\alpha}$, and the quaternion multiplication rule [4], the quaternion update equation is given by

$$\hat{\boldsymbol{q}}^{\,u}_{k+1} = \bar{\boldsymbol{q}}_{k+1} + \frac{1}{2}\Xi(\bar{\boldsymbol{q}}_{k+1})\delta\hat{\boldsymbol{\alpha}}_{k+1} \tag{39}$$

where $\Xi(\bar{\boldsymbol{q}})$ is found from Eq. (2). This updated quaternion is unit-normalized to within first order according to [10], but a brute-force renormalization is performed to insure that $\hat{\boldsymbol{q}}_{k+1}^T\hat{\boldsymbol{q}}_{k+1} = 1$,

$$\hat{\boldsymbol{q}}_{k+1} = \frac{\hat{\boldsymbol{q}}^u_{k+1}}{\|\hat{\boldsymbol{q}}^u_{k+1}\|} \tag{40}$$

The postupdate estimate for the rest of the state vector elements is found by adding the a posteriori estimated error state element to the a priori estimate. The angular velocity estimate is computed from $\hat{\boldsymbol{\omega}}^b_{k+1} = \tilde{\boldsymbol{\omega}}_{k+1} + \Omega_{g_{k+1}}\hat{\boldsymbol{m}}_{g_{k+1}} - \hat{\boldsymbol{\beta}}_{k+1}$.

F. Fixed Interval Smoothing

The multiplicative extended Kalman smoother (MEKS) uses the MEKF from the last section as the forward filter. For the backward smoothing pass, the Rauch–Tung–Striebel (RTS) algorithm [10] for linear discrete-time systems is used on the linearized system. The smoothed quaternion $\hat{\boldsymbol{q}}^u_{k|N}$ is calculated using the equation

$$\hat{\boldsymbol{q}}^{\,u}_{k|N} = \bar{\boldsymbol{q}}_k + \frac{1}{2}\Xi(\bar{\boldsymbol{q}}_k)\delta\hat{\boldsymbol{\alpha}}_{k|N} \tag{41}$$

where $\bar{\boldsymbol{q}}_k$ is the a priori estimate from the forward filter pass, and $\delta\hat{\boldsymbol{\alpha}}_{k|N}$ is the smoothed estimate of the error angles. This smoothed quaternion estimate gets renormalized after this smoothing update, as in Eq. (40).

G. Filter Tuning

The goal of filter tuning is to make the filter converge to an estimated value, and to maximize the accuracy of the estimate. The tuning is done by selection of appropriate values of the process noise spectral density $\tilde{Q}$, the measurement noise covariance R, and the initial filter covariance $\hat{P}_0$. In this work, the diagonal elements of $\hat{P}_0$ are chosen to be the squares of the expected errors in the initial state vector $\hat{\boldsymbol{x}}_0$. All off-diagonal elements are set to zero. The diagonal elements of R are chosen to reflect the expected measurement errors in the attitude sensors, and the off-diagonal elements are set to zero. The first three diagonal elements of $\tilde{Q}$ are chosen to reflect the gyro noise, as determined from preflight evaluation. The rest of the diagonal elements are chosen to be close to zero, to model the parameters as random constants. A very small pseudonoise is added because of the nonoptimality of the extended Kalman filter [13]. All off-diagonal elements of $\tilde{Q}$ are set to zero.

V. Generation of an Initial Estimate that Ensures EKF Convergence

The EKF is a suboptimal filter for this nonlinear system, because it is based on a linearization of the system's nonlinearities. Therefore, the initial attitude estimate must be close to the true attitude to ensure that the filter will converge. A common way to initialize an attitude determination EKF is by using a deterministic method like TRIAD (the algebraic method [4]) or the q-method [4] on the first set of complete vector measurements. This approach ensures that the filter is initialized with an attitude close to the true attitude. Because the sun sensor does not measure the sun pointing vector, but rather a scalar, this method cannot be used directly. One possible solution is to construct a sun vector from the measurement, and use, e.g., TRIAD. A more straightforward approach is to use the sun sensor measurement directly. A direct approach avoids the need to do a complicated geometric reconstruction of the body-axis sun vector based on magnetometer data and on the scalar output of the one-axis sun sensor. Given an attitude (rotation) matrix that maps the unit vector $\hat{\boldsymbol{B}}^{\text{eci}}$ in the direction of the reference-coordinates magnetic field as calculated by the IGRF model into the unit vector $\hat{\boldsymbol{B}}^b$ in the direction of the body-coordinates magnetic field as measured by the magnetometer, the only uncertainty left is the rotation about the measured magnetic field vector. From [14], the quaternion that defines the minimum rotation that satisfies the measurement constraint $\hat{\boldsymbol{B}}^b = A(\boldsymbol{q})\hat{\boldsymbol{B}}^{\text{eci}}$ is given by

$$\boldsymbol{q}_{\min}(\hat{\boldsymbol{B}}^b, \hat{\boldsymbol{B}}^{\text{eci}}) = \begin{cases} \frac{1}{\sqrt{2[1+(\hat{\boldsymbol{B}}^b)^T\hat{\boldsymbol{B}}^{\text{eci}}]}}\begin{bmatrix}\hat{\boldsymbol{B}}^b\times\hat{\boldsymbol{B}}^{\text{eci}}\\ [1+(\hat{\boldsymbol{B}}^b)^T\hat{\boldsymbol{B}}^{\text{eci}}]\end{bmatrix} & \text{if } (\hat{\boldsymbol{B}}^b)^T\hat{\boldsymbol{B}}^{\text{eci}} > -1\\ \begin{bmatrix}\hat{\boldsymbol{v}}\\ 0\end{bmatrix} & \text{if } (\hat{\boldsymbol{B}}^b)^T\hat{\boldsymbol{B}}^{\text{eci}} = -1\end{cases} \tag{42}$$

The vector $\hat{\boldsymbol{v}}$ in Eq. (42) is any unit vector that is perpendicular to $\hat{\boldsymbol{B}}^b$. If one assumes no measurement errors, then the attitude can be represented by

$$\boldsymbol{q}(\theta) = \begin{bmatrix}\hat{\boldsymbol{B}}^b\sin(\theta/2)\\ \cos(\theta/2)\end{bmatrix} \otimes \boldsymbol{q}_{\min}(\hat{\boldsymbol{B}}^b, \hat{\boldsymbol{B}}^{\text{eci}}) \tag{43}$$

where θ is a rotation about the measured magnetic field vector. The angle θ must be determined to find a good initialization. This is done by calculating $\boldsymbol{q}(\theta)$ for a grid of θ values in the range of 0–2π and comparing the modeled output from the sun sensor (with all calibration error terms set equal to zero) with the measurement from the sun sensor. A θ grid spacing of 0.01 deg was chosen. The attitude quaternion corresponding to the θ value, resulting in the smallest difference between the modeled and measured sun sensor output, is used as the filter's initial attitude guess.

The accuracy of this algorithm is dependent on how large the actual sensor calibration errors are. In addition, invalid telemetry sensor data can occur, and this could cause the calculated initial attitude to be too far from the true attitude. Because this estimator is used for postflight attitude reconstruction, it should be sufficient to monitor the filter innovations to determine whether a reasonable initialization has occurred. The normalized innovation squared (NIS) could be calculated (see next section), and large/unexpected NIS values could be taken as an indication of a bad filter initialization, and

an alternate sample could be used for filter initialization in that case. Unreasonable calibration parameter estimates combined with lack of convergence also indicate that something is wrong. In addition, sensor data validation should be performed, e.g., by scalar checking, before sensor data are input to the estimation algorithm [4].

VI. Evaluation of Filter and Smoother Performance

A. Consistency Testing

The filter and smoother developed in this paper underwent consistency checks using data from a truth-model simulation to evaluate their performance. As given by Bar-Shalom et al. [13], the normalized state estimation error squared (NEES) can be used to verify that the estimates can be accepted as consistent. A consistent estimate is unbiased (zero-mean estimation error), and the actual mean-square error (MSE) matches the filter/smoother calculated covariance. The NEES is defined by the quadratic form $\epsilon_k = \boldsymbol{e}_k^T \hat{P}_k^{-1} \boldsymbol{e}_k$, where $\boldsymbol{e}_k = \boldsymbol{x}_k - \hat{\boldsymbol{x}}_k$ and $\hat{P}_k$ is the filter/smoother calculated covariance. From N Monte Carlo simulation runs, the ensemble average NEES is computed as

$$\bar{\epsilon}_k = \frac{1}{N} \sum_{i=1}^{N} \epsilon_k^i \tag{44}$$

Given a consistent estimator, $N\bar{\epsilon}_k$ is χ^2 (chi-square) distributed with Nn_x degrees of freedom, where n_x is the dimension of the state vector. Then, $\bar{\epsilon}_k$ tends toward n_x as N approaches infinity. The acceptance interval of the consistency test is determined from the 95% confidence interval of the χ^2 distribution.

To check that the filter is working properly also when real sensor data are used, a single-run (real-time) consistency test can be performed [13]. This test analyzes the properties of the filter innovation $\boldsymbol{\nu}_k = \boldsymbol{z}_k - H_k \bar{\boldsymbol{x}}_k$, where $\bar{\boldsymbol{x}}_k$ is the a priori filter state at sample k. For the filter to be consistent, the innovation should be zero mean and white. The normalized innovation squared (NIS) is defined as $\epsilon_{\nu_k} = \boldsymbol{\nu}_k^T S_k^{-1} \boldsymbol{\nu}_k$, where the innovation covariance S_k is given by $S_k = H_k \bar{P}_k H_k^T + R_k$ and $\bar{P}_k$ is the filter's a priori covariance matrix at sample k. To test the statistical properties of the innovation, the time-averaged NIS is calculated by

$$\bar{\epsilon}_\nu = \frac{1}{K} \sum_{k=1}^{K} \boldsymbol{\nu}_k^T S_k^{-1} \boldsymbol{\nu}_k \tag{45}$$

where K is the number of samples. If the Kalman filter model is correct, then $K\bar{\epsilon}_\nu$ is sampled from a chi-squared distribution of degree Kn_z, where n_z equals the dimension of the measurement vector.

The whiteness test for the innovations for a single run using K data points can be written as the time-averaged autocorrelation [10]

$$\bar{\rho}_j = \frac{\frac{1}{\sqrt{n_z}} \sum_{k=1}^{K} \boldsymbol{\nu}_k^T \boldsymbol{\nu}_{k+j}}{\sqrt{\sum_{k=1}^{K} \boldsymbol{\nu}_k^T \boldsymbol{\nu}_k \sum_{k=1}^{K} \boldsymbol{\nu}_{k+j}^T \boldsymbol{\nu}_{k+j}}} \tag{46}$$

where j is the lag distance index. The acceptance region is given by [10]

$$\bar{\rho}_j \in \left[\frac{-1.96}{\sqrt{K}}, \frac{1.96}{\sqrt{K}} \right] \tag{47}$$

B. Observability

The system observability can be investigated locally by calculating the observability Gramian [1] for the linearized, time-varying system, using data from the whole flight or from part of the flight. The observability Gramian is given by

$$\vartheta = \sum_{k=1}^{N} \Phi^T(t_k, t_0) H_k^T H_k \Phi(t_k, t_0) \tag{48}$$

where $\Phi(t_k, t_0)$ is the state transition matrix from time t_0 to time t_k, and H_k is the Jacobian matrix of the nonlinear measurement function $\boldsymbol{h}_k(\boldsymbol{x}_k)$. The linearized system is observable if the observability Gramian matrix is nonsingular (i.e., if the rank of the observability Gramian matrix is equal to the number of states in the system).

The condition number based on singular value decomposition (SVD) is used to get an idea of how good the observability is [10]. A matrix is singular if its condition number is infinite, and a large condition number indicates a nearly singular matrix. The minimum value of the condition number is unity, and a small condition number can be interpreted as an indication of good observability. A small condition number means small compared to the reciprocal of the machine's floating-point precision [15], which is about 10^{15} in IEEE double precision.

Any single TAM measurement provides only two axes of attitude information, and the rotation about the measured vector cannot be resolved. A series of TAM measurements can, under certain conditions, make the three-axes attitude observable [2]. The important point here is that large movement of $\hat{\boldsymbol{B}}^{\text{eci}}$ makes the attitude observable, whereas a very small movement results in weak observability. In the present application, with sounding rockets with short flight time, the observability from the TAM alone would be very poor. Therefore, sun sensor measurements are necessary to get good attitude observability. Relative misalignment calibration of the TAM and sun sensor with respect to the gyro axes has been used in this work to make the system observable. As pointed out in [3], absolute misalignment is not observable from attitude sensors alone.

VII. Simulation Results

The truth models used in the simulations contain the true attitude and rate time histories. Simulated IRU, TAM, and sun sensor (DSS) measurements are generated, including sensor errors and noise. The simulated data are then fed into the estimator, which produces an estimate of the rocket attitude and rate time history along with the calibration parameters of the attitude sensors. At time points without sun sensor measurements, the filter runs the measurement update equations with the sun sensor row of the measurement matrix H set to zero. When the first valid sun measurement is detected, the initialization algorithm calculates the attitude estimate used to initialize the filter.

The generation of the truth-model measurements is a multistep process. First, the trajectory of the rocket is constructed. From the geocentric positions of the rocket and the time, the magnetic field vector time history $\boldsymbol{B}^{\text{eci}}[\boldsymbol{r}^{\text{eci}}(t), t]$ in the ECI reference frame is computed. $\boldsymbol{B}^{\text{eci}}$ depends directly on time because of the IGRF model's coefficient rate terms, which are used to correct for the predicted field drift that occurs over the time span since the last model update, and because of the Earth's rotation. In addition, $\boldsymbol{B}^{\text{eci}}$ depends on time indirectly through the rapid dependence of the rocket position on time as it moves along its trajectory $\boldsymbol{r}^{\text{eci}}(t)$. The $\hat{\boldsymbol{S}}^{\text{eci}}$ unit pointing vector to the sun in the ECI frame is calculated for each time point using the formula in the Astronomical Almanac [9]. In this formula, $\hat{\boldsymbol{S}}^{\text{eci}}$ depends only on time. (For very accurate sun positions this vector also depends on the spacecraft position [16].) From the rate time history, the true quaternion time history $\boldsymbol{q}$ is generated, using the discrete propagation $\boldsymbol{q}_{k+1} = \exp[\frac{1}{2}\Omega(\boldsymbol{\omega}_k)\Delta T]\boldsymbol{q}_k$. The gyro measurements $\tilde{\boldsymbol{\omega}}$ in the IRU frame are computed from the true angular rates $\boldsymbol{\omega}^b$ in the body frame by the relation $\tilde{\boldsymbol{\omega}} = S_g^{-1}(\boldsymbol{\omega}^b + \boldsymbol{\beta} + \boldsymbol{\eta}_v)$. The magnetometer measurements $\tilde{\boldsymbol{B}}$ and the sun sensor measurements $\tilde{x}_c$ are computed from the magnetometer model and the sun sensor model, respectively. A sun visibility check is also included to reject sun sensor measurements when the sun is outside the field of view of the sun sensor. In addition, the sun sensor measurements are down-sampled to match the spin frequency of the rocket, giving one sun sample per spin.

The time correlation of the Earth's magnetic field model error is modeled in the truth-model simulation by a first-order Gauss–Markov process. This is added to the output from the IGRF model. In addition, a bias of 50 nT is added to the truth model. The reason for

including this in the truth model of the Earth's magnetic field is to verify that the filter is working properly with realistic IGRF modeling errors.

The following model parameters have been used in the simulator: The nonorthogonal misalignments of the gyros are $\boldsymbol{\varepsilon} = [0.4 \;\; 0.6 \;\; -0.6]^T$ deg. The Gyro bias vector is $\boldsymbol{\beta} = [1 \;\; 0.5 \;\; 0.7]^T$ deg/s, and the gyro scale-factor errors are $\boldsymbol{\lambda}_g = [17.5 \;\; 8.7 \;\; 12.2]^T \cdot 10^{-3}$. The square roots of the power spectral densities of the rate white-noise processes of the gyros are $[\sigma_{v_x} \;\; \sigma_{v_y} \;\; \sigma_{v_z}]^T = [1.4 \;\; 0.3 \;\; 0.3]^T$ deg/$\sqrt{\text{s}}$. The orthogonal misalignments of the sun sensor are $\phi_s = 0.7$ deg, $\theta_s = -0.7$ deg, and $\psi_s = 0.5$ deg. The sun sensor bias is $b_s = 3$ pixels, and the sun sensor scale-factor error is $\delta e = -28.6$ pixels. The standard deviation of the sun sensor white noise is $\sigma_{\text{DSS}} = 1.5$ pixels. The misalignments of the magnetometer are $\delta_{xy} = 1$ deg, $\delta_{xz} = 1.3$ deg, $\delta_{yz} = 1.5$ deg, $\delta_{yx} = 0.8$ deg, $\delta_{zx} = 1.0$ deg, and $\delta_{zy} = 1.2$ deg. The magnetometer bias vector is $\boldsymbol{b} = [100 \;\; 130 \;\; 150]^T$ nT, and the magnetometer scale-factor errors are $\boldsymbol{\lambda}_m = [3 \;\; 2.5 \;\; 3.5]^T \cdot 10^{-3}$. Finally, the standard deviations of the magnetometer random measurement errors are $\sigma_{\text{TAM}} = 190$ nT.

A. Test Case 1

To verify correct behavior of the filter and smoother, a "rich" rocket motion time history has been used in this test case. This type of motion is the most likely to produce observability of the calibration parameters; thus, observability in this case is a necessary condition for the sensibility of the estimator. At the outset of this work, it was not clear that all of the calibration parameters would be simultaneously observable along with the attitude even with the use of misalignment parameters that are defined relative to the IRU axes. This uncertainty arose because of the newness of the sun sensor model and of its calibration parameter set. Therefore, an important part of the truth-model study of this system has been to consider whether the calibration parameters are all observable.

IRU and TAM data have been generated with a sample rate of 200 Hz. During the first 65 s of the simulation, no sun sensor measurements are available. To construct a rich motion, a sinusoidal attitude rate oscillation in all three axes was selected, with amplitudes of 1000, 500, and 500 deg/s that varied at 4, 0.1, and 0.15 Hz in the roll, pitch, and yaw axes, respectively. This is a very unrealistic motion for a spin-stabilized sounding rocket, but the main point of this test case was to verify the filter design and the observability of all the calibration parameters. The rank of the observability Gramian matrix for this simulation run was 29, meaning that the system is observable. The condition number of the Gramian matrix was about $7.1 \cdot 10^6$, and all of the 26 calibration parameter estimates converged very closely to their true values. The total attitude error can be seen in Fig. 2.

Figure 2 shows a large transient at about 65 s, corresponding to the time of the first valid sun sensor measurement. After the initial transient, the filter converges very rapidly because of a relatively good observability. It converges to an absolute attitude error with a mean value of about 0.2 deg. The total attitude error is less than 1 deg after $t = 67$ s, which is within the target accuracy for this system.

The EKF is not an optimal estimation algorithm due to various inconsistencies between the filter and the actual truth model. Therefore, it will in general not give consistent estimates for the parameters. In addition, the estimates will not converge to the exact true values [13]. Pseudonoise can sometimes be added to the process noise covariance matrix to make the filter consistent, and this was verified by Monte Carlo simulations and NEES calculations. If a correlated and biased IGRF model is used in the truth-model simulations, the TAM scale-factor estimates do not converge exactly to the true values because of the mismatch between the filter model and the truth model. Because of the model mismatch, the NEES consistency test is not passed.

B. Test Case 2

The simulation in the previous section verified the estimator during an "ideal" situation with respect to observability. What is more interesting is to look at the estimator performance for a realistic flight of a spin-stabilized sounding rocket. The simulation in this section is based on the rate time history and the trajectory of the IMEF (Investigation of Middle Atmosphere Electric Field Fluctuations) sounding rocket, launched from Andoya Rocket Range in July 2005. This was a spin-stabilized rocket without a despin unit, and the flight time was about 300 s. Its average spin rate was about 6 rps. Simulated IRU and TAM data have been generated with a sample rate of 200 Hz. During the first 65 s of the simulation, no sun sensor measurements are available. This is because the sun sensor is located under the nose cone, and the nose cone is ejected at about 65 s. One sun measurement is generated per spin period, and this gives 1255 valid sun measurements during the simulation run.

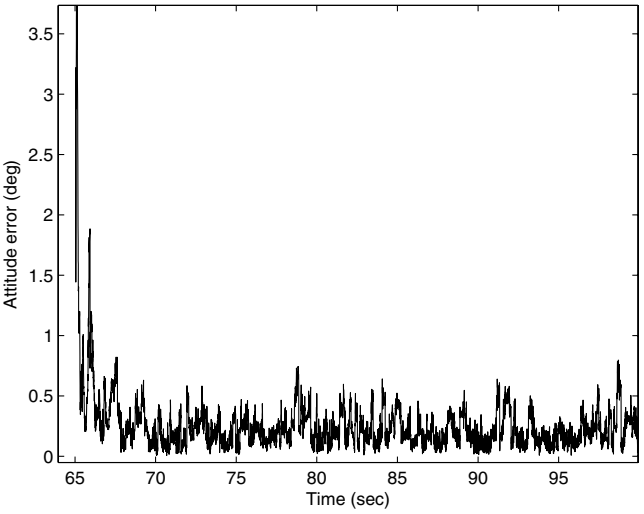

Fig. 2 Filter attitude error time history for test case 1.

In general, a sinusoidally varying angular rate in each axis would be good for the calibration parameter observability, but this normally cannot be achieved about all three axes. For a sounding rocket, sinusoidal yaw and pitch rate variations usually occur due to nutations, but they may be very small. The roll-axis angular velocity will be very large at first, but it will most likely decrease because of energy dissipation in semirigid boom systems. The resulting decay in the roll rate is usually slow at first, but it may accelerate toward the end of the flight if the corresponding nutations become very large. If this deceleration occurs, then the yaw and pitch sinusoidal oscillations will increase in amplitude toward the end of the flight. The initial slow variation of the roll rate and the initial small yaw and pitch rates tend to decrease the observability of several of the calibration parameters because the resulting attitude rate time history does not adequately probe the space of all possible attitude rates. In addition, the rocket is often launched almost parallel to the magnetic field lines. Therefore, the x axis of the TAM (longitudinal axis) may experience a large field, but only modest variations. On the other hand, the TAM y axis and z axis experience smaller fields, but with large variations. If the yaw and pitch nutations become large while the roll rate becomes small at the end of the flight, then the observability of the calibration parameters may be increased. Figure 3 depicts the angular velocity profile used in this simulation.

The angular rate time history is based on the rate measurements from the IRU onboard the IMEF payload. The IRU was sampled with a frequency of 1085 Hz on this flight. Sample rate alteration was used to down-sample the IRU data to 200 Hz, and these smoothed rate measurements [using the Savitzky–Golay finite impulse response (FIR) smoothing filter [15]] were used as the true angular rates. In this simulation, IGRF modeling errors were added using a bias of 50 nT and a first-order Gauss–Markov process. This Gauss–Markov process gives an additional systematic change in the modeled magnetic field of about 50 nT during the flight time. The rocket's pitch and yaw rates were very low for most of the flight, with amplitudes of about ± 2 deg/s. This small sinusoidal motion was caused by the initial small nutation level. Energy dissipation in

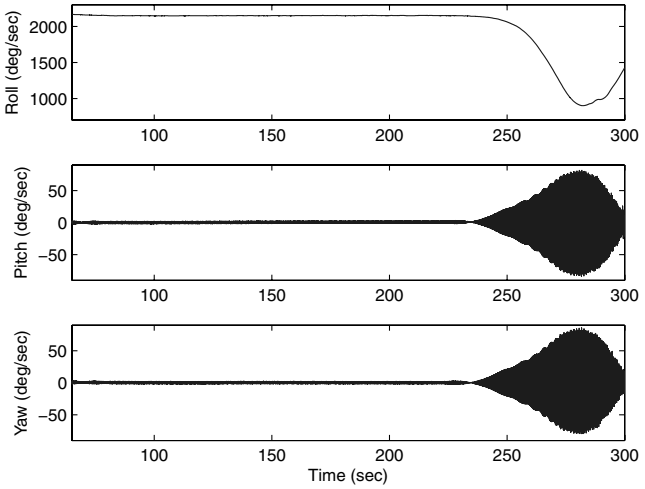

Fig. 3 Angular velocity profile for test case 2.

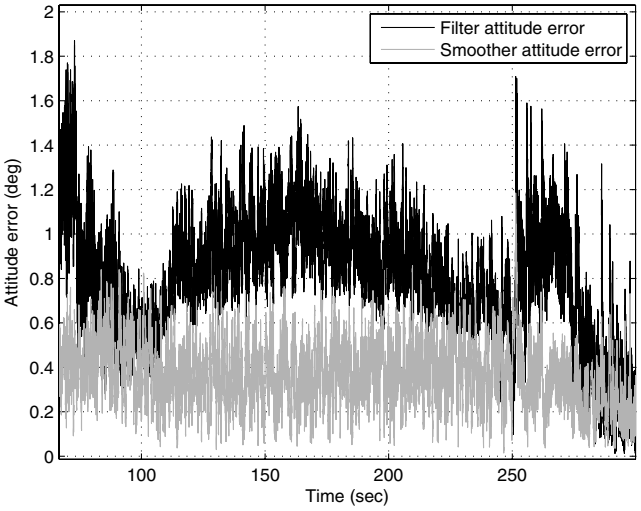

Fig. 4 Filter and smoother attitude error time history for test case 2.

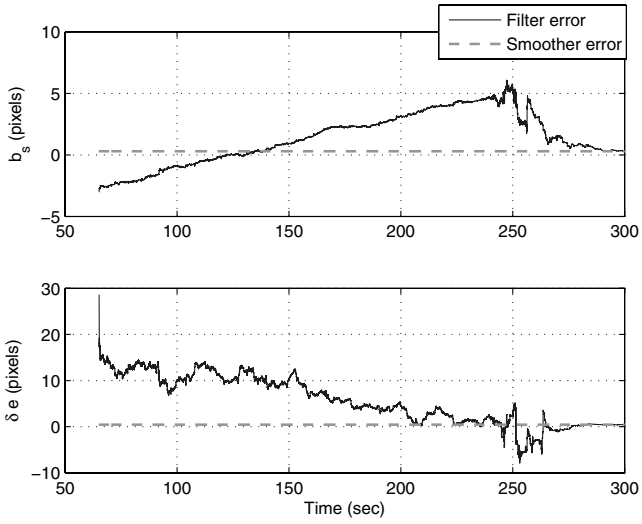

Fig. 5 Filter and smoother estimation errors for the sun sensor bias and scale-factor, test case 2.

flexible boom systems makes a minor-axis spinner, such as a spin-stabilized sounding rocket, unstable with time, and this causes the nutations to increase [4]. However, a failure caused the IMEF nose cone never to be ejected, and the boom system onboard was never deployed. The result of this was a very stable (not decreasing) roll rate during most of the flight, and no significant increase in the nutation in this time period. After 240 s, the roll rate dropped and the nutation increased when the rocket reentered the dense atmosphere with the motor still attached to the payload. The yaw and pitch amplitudes increased up to about ± 80 deg/s. The combination of high spin velocity, short flight time, and relatively small nutation for most of the flight should make this simulation appropriate as a "worst-case" performance indication for the estimator.

The rank of the observability Gramian matrix for this simulation run was still 29, meaning that the system is observable. The condition number of the Gramian matrix was increased to $3.28 \cdot 10^{13}$, indicating weak observability in this case. This means that, for a fast spinning sounding rocket with little nutation, the parameter observability may not be very good. However, the simulation indicates that, even in this case, many of the calibration parameters are estimated accurately, and almost all of the calibration parameter estimates show significant improvement compared with their a priori values.

Filter and smoother attitude error results are shown in Fig. 4 for this test case. This figure shows that the smoother achieves a total attitude error with a mean value of about 0.4 deg and a peak value below 0.8 deg throughout the simulation run. As expected, the filter is less accurate, and it displays an initial error transient, but its accuracy is sufficient to ensure that its linearized models are reasonable. The attitude and calibration parameter errors remained within or very close to their respective 3σ bounds, which indicate that the filter/smoother is working properly. The time-averaged NIS test (performed on the last 2000 samples, corresponding to the last 10 s of the simulation run) was outside the acceptable range, but the innovations were within the acceptance range for the whiteness test (when a small pseudonoise was added to the process noise covariance matrix).

Filter and smoother estimation errors for the sun sensor bias and scale-factor error are shown in Fig. 5. It is evident from these results that the increased nutation at the end of the flight makes the parameters more observable and the estimates more accurate. The sun sensor bias estimate seems to diverge before the increased nutation at the end of the flight. The smoothed estimates are constant throughout the simulation run, as expected, because the calibration parameters are modeled as random constants.

The in-flight estimation of the 26 sensor calibration parameters improves the performance of the attitude estimator. Therefore, this 29-state attitude determination and in-flight calibration filter should perform much better than a basic six-state filter [6], where only three rate-gyro biases are estimated in addition to the attitude. To compare the 29-state filter developed in this work with the basic six-state filter, the 29-state filter was run with all of the initial covariances of the calibration parameters set to be very small values, except for those associated with the rate-gyro biases. This latter run produces results that are essentially identical to those that would be produced by a standard six-state filter. Figure 6 shows the filtered total attitude error time history for this run. A comparison of this time history to the filtered time history in Fig. 4 shows that the 29-state filter exhibits much better performance than does the six-state filter. The six-state filter reached a mean total attitude error of about 4 deg during most of the flight. The 29-state filter reached a mean value of about 1 deg or less during most of the flight, and this corresponds to an accuracy improvement by a factor of four or more. As expected, the NIS test is very far from being passed by the six-state filter because of the large calibration modeling errors that are present in this case.

C. Test Case 3

The Cleft Accelerated Plasma Experimental Rocket (CAPER) was launched from Andoya Rocket Range in January 1999. The flight lasted longer than 1300 s and reached an apogee altitude of 1360 km. The truth-model quaternion and rate time histories used in this last simulation case are based on the outputs of the smoother used to calculate the actual attitude and rate time histories for the CAPER sounding rocket flight. This smoother is described in [17]. This case's "truth" attitude quaternion history has been generated by discrete propagation of the truth rates from the study of [17]. The first

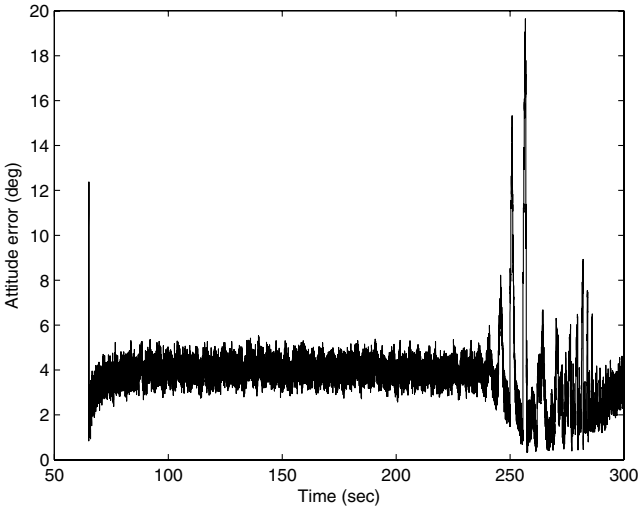

Fig. 6 Attitude error time history for the basic six-state filter in test case 2.

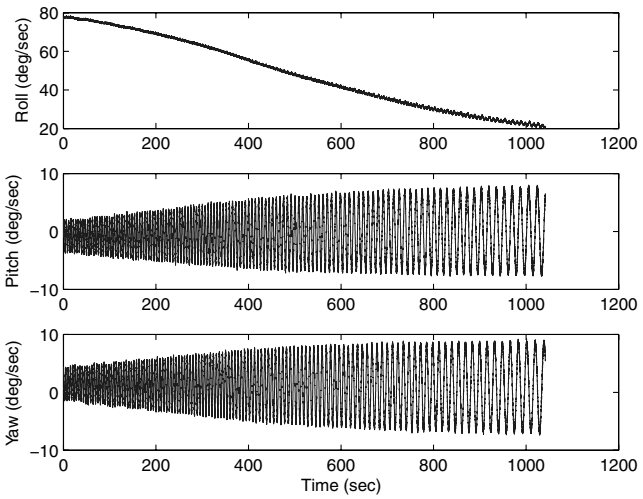

Fig. 7 IRU measurement time histories for the CAPER flight simulation.

quaternion estimate from the Psiaki et al. [17] smoother was used as the initial truth attitude for this case. The simulated IRU measurements for this test case are shown in Fig. 7.

IRU and TAM data have been generated at a sample rate of 20 Hz, and the sun sensor visibility model has generated one sun measurement per spin period, when the sun sensor had its field of view in the direction of the sun. This approach has resulted in 133 valid sun measurements during the simulation run. The time used in this simulation has been defined starting from $t = 0$ at the sample time of the first rate and quaternion estimates provided by the smoother of [17]. The first sample time corresponds to about 181 s after launch, and the last sample time corresponds to about 1223 s after launch. As time progresses, the amplitude of the pitch and yaw nutation grows, and the magnitude of the spin rate about the roll axis decreases. The data that were provided from the CAPER flight had a sample rate of about 5.3 Hz, and interpolation was used to create rate data with a sample rate of 20 Hz. The relatively low spin rate of this simulated rocket flight means that gyros with a smaller dynamic range could be used on all three IRU axes, and this gives a smaller gyro noise. Therefore, in this simulation, the square root of the gyro noise spectral density for each axis has been set to 0.2 deg $/\sqrt{\text{s}}$.

The rank of the observability Gramian matrix for this simulation run was 29; therefore, the system is observable. The condition number of the Gramian matrix was $9.73 \cdot 10^{10}$, indicating better observability than in test case 2. The total attitude error time histories

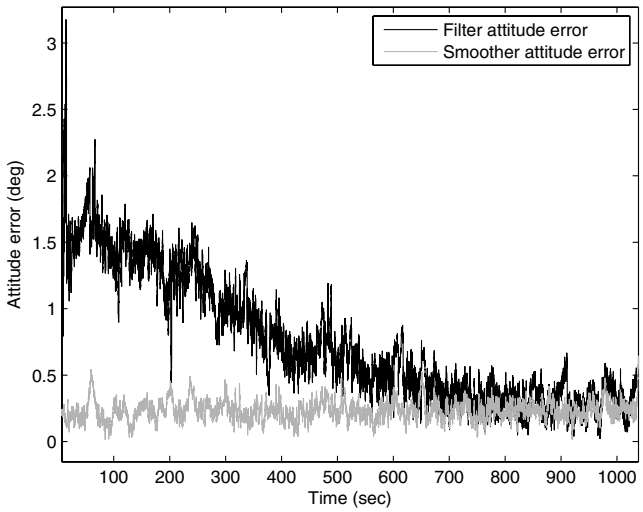

Fig. 8 Filter and smoother attitude error time histories for test case 3.

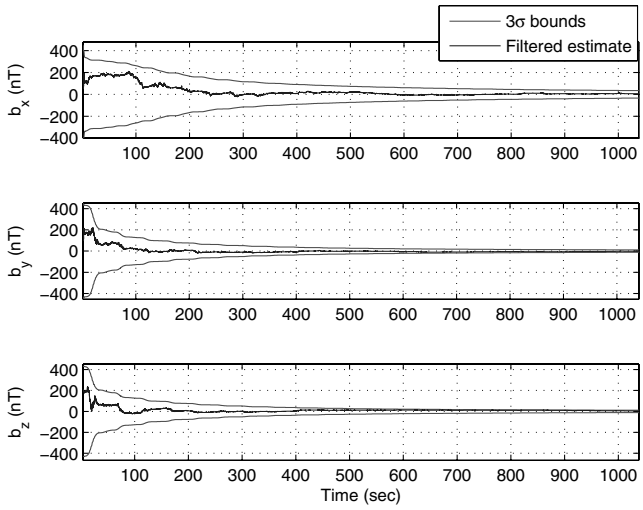

Fig. 9 Filter TAM bias estimation error time history for test case 3.

of the filter and the smoother for this test case are plotted in Fig. 8. This figure shows that the smoother's total error has a mean value of about 0.25 deg and a peak of about 0.5 deg. The filter's estimation error time histories for the three TAM biases are presented in Fig. 9, along with the filter's computed estimates of their 3σ bounds. The convergence of these calibration errors to small values provides a further verification of the success of this in-flight calibration procedure, which is the result of the system's observability.

IGRF modeling errors have been added to test the estimator. A bias of 50 nT and a first-order Gauss–Markov process with a correlation time of 500 s and a white-noise standard deviation of 0.4 nT have been added to the output of the IGRF model before its input to the estimator. The observed attitude accuracy was not significantly degraded by this systematic modeling error.

VIII. Conclusions

A gyro-based attitude determination and sensor calibration extended Kalman filter and smoother have been developed for sounding rockets using low-cost MEMS gyros, a TAM, and a new digital sun sensor. The filter is initialized in a way which ensures that it converges: by searching in the space of rotations about the measured magnetic field vector for the angle that best matches the sun sensor scalar measurement. For postflight scientific data analysis, the smoother is run after the filter in a noncausal RTS-type backward pass to refine the filter's attitude and rate estimates. For fast spinning rockets, a very high roll rate compared to low pitch and yaw

rates results in weaker observability for some calibration parameters if the pitch and yaw nutation amplitudes remain small throughout the flight. This can happen if the minor-axis stabilized rocket only has short, rigid booms that do not dissipate much energy. A "richer" payload nutational motion with large coning angles toward the end of the flight results in improved observability of the sensor calibration parameters, and these improvements tend to result in improved attitude accuracy as well. Truth-model simulations indicate that the 29-state attitude-determination/in-flight-calibration system is observable under normal circumstances and that a 3-σ attitude accuracy of 0.5–1 deg can be achieved.

Acknowledgments

The first author would like to thank Cornell University for providing tuition money for a visit to the Sibley School of Mechanical and Aerospace Engineering for the Fall 2005 semester. This project has received financial support from the Norwegian Research Council and Andoya Rocket Range. The attitude estimation algorithms developed in this work are part of the Sounding Rocket Attitude Determination System project at the University of Oslo.

References

[1] Psiaki, M. L., Martel, F., and Pal, P. K., "Three-Axis Attitude Determination via Kalman Filtering of Magnetometer Data," *Journal of Guidance, Control, and Dynamics*, Vol. 13, No. 3, 1990, pp. 506–514.

[2] Humphreys, T. E., Psiaki, M. L., Klatt, E. M., Powell, S. P., and Kintner, P. M., "Magnetometer-Based Attitude and Rate Estimation for Spacecraft with Wire Booms," *Journal of Guidance, Control, and Dynamics*, Vol. 28, No. 5, 2005, pp. 584–593.

[3] Pittelkau, M. E., "Kalman Filtering for Spacecraft System Alignment Calibration," *Journal of Guidance, Control, and Dynamics*, Vol. 24, No. 6, 2001, pp. 1187–1195.

[4] Wertz, J., *Spacecraft Attitude Determination and Control*, Kluwer Academic, Norwell, MA, 1978, pp. 328–331, 414–416, 424–428, 501–502, 564, 758–759.

[5] Kuipers, J. B., *Quaternions and Rotation Sequences: A Primer with Applications to Orbits, Aerospace and Virtual Reality*, Princeton Univ. Press, Princeton, NJ, 1999.

[6] Lefferts, E. J., Markley, F. L., and Shuster, M. D., "Kalman Filtering for Spacecraft Attitude Estimation," *Journal of Guidance, Control, and Dynamics*, Vol. 5, No. 5, 1982, pp. 417–429.

[7] Shuster, M. D., Pitone, D. S., and Bierman, G. J., "Batch Estimation of Spacecraft Sensor Alignments 1: Relative Alignment Estimation," *Journal of the Astronautical Sciences*, Vol. 39, No. 4, 1991, pp. 519–546.

[8] Pittelkau, M. E., "Everything is Relative in Spacecraft System Alignment Calibration," *Journal of Spacecraft and Rockets*, Vol. 39, No. 3, 2002, pp. 460–466.

[9] *Astronomical Almanac for the year 2006*, U.S. Nautical Almanac Office, Washington, D.C., 2006, p. C24.

[10] Crassidis, J. L., and Junkins, J. L., *Optimal Estimation of Dynamic Systems*, Chapman Hall/CRC, Boca Raton, FL, 2004, pp. 274, 303, 351–355, 419–427.

[11] Markley, F. L., "Attitude Error Representation for Kalman Filtering," *Journal of Guidance, Control, and Dynamics*, Vol. 26, No. 2, 2003, pp. 311–317.

[12] Gelb, A., *Applied Optimal Estimation*, MIT Press, Cambridge, MA, 1979.

[13] Bar-Shalom, Y. B., Li, X. R., and Kirubarajan, T., *Estimation with Applications to Tracking and Navigation*, Wiley, New York, 2001, pp. 232–245, 395–396, 481–482.

[14] Reynolds, R. G., "Quaternion Parameterization and a Simple Algorithm for Global Attitude Estimation," *Journal of Guidance, Control, and Dynamics*, Vol. 21, No. 4, 1998, pp. 669–671.

[15] Press, W., Flannery, B., Teukolsky, S., and Vetterling, W., *Numerical Recipies in C: The Art of Scientific Computing*, Cambridge Univ. Press, New York, 2nd ed., 1992, pp. 59–71, 650–655.

[16] Psiaki, M. L., "Autonomous Low-Earth-Orbit Determination from Magnetometer and Sun Sensor Data," *Journal of Guidance, Control, and Dynamics*, Vol. 22, No. 2, 1999, pp. 296–304.

[17] Psiaki, M. L., Klatt, E. M., Kinter, P. M., and Powell, S. P., "Attitude Estimation for a Flexible Spacecraft in an Unstable Spin," *Journal of Guidance, Control, and Dynamics*, Vol. 25, No. 1, 2002, pp. 88–95.